Advanced Composites and Hybrid Materials (2022) 5:130–143
https://doi.org/10.1007/s42114-021-00361-7

ORIGINAL RESEARCH

Magnetically sensitive and high template affinity surface imprinted polymer prepared using porous TiO_2-coated magnetite-silica nanoparticles for efficient removal of tetrabromobisphenol A from polluted water

Yanming Shao[1] · Hao Bai[1] · Haihua Wang[1,2] · Guiqiang Fei[1] · Lulu Li[1] · Ying Zhu[1]

Received: 12 September 2021 / Revised: 4 October 2021 / Accepted: 5 October 2021 / Published online: 3 November 2021

Abstract
Tetrabromobisphenol A (TBBPA) has been considered as one of the persistent organic pollutants in water. It is urgent to determine TBBPA in environment due to its detriment to humans and aquatic species. However, sample pretreatment prior to instrumental analysis is always required because of the low concentration of TBBPA and the complexity of the matrix. A novel molecularly imprinted polymer (MIP) was prepared using magnetic mesoporous TiO_2 as matrix. The mesoporous TiO_2 layer could provide sufficient recognition sites for MIP, and Fe_3O_4 core can facilitate its separations from liquid medium. After azido was introduced onto Fe_3O_4@mTiO_2 by non-covalent effect, alkynyl-terminated reversible addition – fragmentation chain transfer (RAFT) agent was fixed by click chemistry. The MIP was prepared via RAFT polymerization in the presence of TBBPA using 4-vinylpyridine (4-VP) and ethyleneglycol dimethacrylate (EGDMA) as functional monomer and crosslinker, respectively. The adsorption process reached equilibrium within 20 min. The maximum adsorption capacity of MIP for TBBPA at an ideal ratio of 4-VP and EGDMA was 41.67 mg g^{-1} and was much higher than that of non-imprinted polymer (20.92 mg g^{-1}). The MIP also exhibits excellent affinity towards TBBPA in the presence of structural analogs. Additionally, the as-prepared MIP can be repeatedly reused due to the magnetic core.

Keywords Magnetic porous TiO_2 · Azido-functionalized dopamine · SI-RAFT polymerization · Surface molecular imprinted polymers · Tetrabromobisphenol A

1 Introduction

Brominated flame retardant (BFR) has been widely used in plastics and textiles such as electronics, furniture, and clothing [1]. TBBPA, as one of the most ordinary BFR is mostly used as a reactive component in phenolic resins and polycarbonate. Lower grades of TBBPA are also used in epoxy for printed circuit boards, which means that it is incorporated into the polymer backbone [2]. However, as a persistent toxic environmental pollutant and already detected in sewage, sediment, wildlife, and human serum, TBBPA has adverse effects on nature and the human health [3, 4]. Recent researches have also shown that the relative venomous of TBBPA shows a greater potency than its derivatives [5]. The detection of the TBBPA in various matrices has attracted international attention in the last few years.

Based on gas chromatography or high-performance liquid chromatography (HPLC) and other related technologies, sensitive and reliable methods such as liquid chromatography tandem mass spectrometry, gas chromatography-electron capture negative ionization mass spectrometry, and gas chromatography tandem mass spectrometry solid-phase extraction have been developed for the detection of tracing TBBPA [6, 7]. Sample processing procedures prior to instrumental

✉ Yanming Shao
shaoyanming@sust.edu.cn

✉ Haihua Wang
whh@sust.edu.cn

[1] College of Chemistry and Chemical Engineering, Key Laboratory of Auxiliary Chemistry and Technology for Chemical Industry, Ministry of Education, Shaanxi Key Laboratory of Chemical Additives for Industry, Shaanxi University of Science and Technology, Xi'an, Shaanxi 710021, People's Republic of China

[2] College of Chemical Engineering, Shaanxi Institute of Technology, Xi'an 710300, China

analysis are often critically required, because of the entanglement of the environmental matrix and the low concentration of TBBPA.

Molecularly imprinted polymers exhibit excellent affinity towards target molecule because of the presence of the cavity that matches well with the size and force between the target molecule [8]. Therefore, MIP was commonly used for catalysis, separation, solid-phase extraction, and sensing [9, 10]. Applying molecular imprinting techniques to detect TBBPA will be very promising because of its powerful molecular recognition capabilities [11]. However, conventional methods for preparing molecular polymer based on bulk polymerization or precipitation polymerization have some inconveniences, such as the leakage of the template and the incorporation of the binding cavity deeply into the polymer matrix result in the template being difficult to elute, fewer recognition sites, and poor accessibility, which in turn exhibits poor imprinting effect [12].

The surface molecularly imprinted polymer can effectively avoid the above shortcomings of imprinted polymer obtained by the conventional polymerization method because its recognition site is immobilized on the exterior of the carrier. The recognition site and the binding cavity are only locked on the surface of the polymer, which improves the accessibility of the recognition site and the mass transfer rate and enhances the efficiency of the imprinting [13]. Generally, polystyrene nanoparticles, silica nanoparticles, and magnetic ferro ferric oxide nanoparticles are used as support for MIP layer [14–17].

Among many selectable carriers, magnetic nanoparticles have the most potential for application. Their outstanding advantages enable the imprint material to be quickly and efficiently isolated by an external magnetic field without other complicated operations [18]. However, magnetic nanoparticles are easy to be oxidized and unstable in acidic environments, and it is generally required to functionalize them to prepare core–shell imprinted polymers conveniently.

The mesostructured support should be the optimum choice in terms of effectively reducing the response time and increasing the sensitivity of the imprinted polymer due to its well-defined channel structure. The well-organized pore structure allows it to have higher specific surface area, thereby possessing more binding sites and improving the binding ability of the imprinted material [19]. Mesoporous silica and metal organic framework were conventional choice owing to their adjustable pore structure [20, 21]. Xie et al. prepared molecularly imprinted polymer using magnetic mesoporous silica as supports, and the obtained imprinted polymer exhibited excellent performance for detecting protocatechuic acid. The maximum adsorption capacity was 2.3 times than the imprinted material prepared using nonporous supports under the same conditions [21]. The results inform that mesoporous support can effectively improve the recognition properties of as-prepared imprinted polymer and it could be an ideal support for surface imprinted polymer.

The chain transfer reaction is inevitable in the conventional radical polymerization system which resulted in the decreased polymerization degree and the uncontrollable structure of the obtained polymer. Controlled/living radical polymerization (CLRP) can overcome the disadvantages of traditional free radical polymerization and can better control the molecular structure. As one of the most used CLRP, the RAFT polymerization can not only maintain a narrow molecular weight distribution and a mild polymerize conditions, but also no metal ions residue in the polymer matrix. More importantly, it provides a convenient approach for later modification of as-prepared MIP by subsequent polymerization using another functional monomer which will broaden the application filed of MIP [22]. Benefiting from the advantages that mentioned above, RAFT polymerization was used to prepare multifunctional MIP as an attractive approach [23, 24].

In this study, the advantages of magnetic nanospheres, mesoporous supports, and RAFT polymerization were combined to prepare TBBPA imprinted MIP for efficiently detect TBBPA. To the best of our knowledge, TBBPA-related MIP was generally prepared by sol–gel method in the previous work, construction of TBBPA imprinted MIP based on combining the advantages of RAFT polymerization, and magnetic mesoporous support has never been reported [1, 5]. Magnetic mesoporous nanoparticles were firstly prepared using Fe_3O_4 as core, non-porous SiO_2 as inner protecting layer and mesoporous TiO_2 as outer layer which will provide sufficient recognition site for MIP. Azido was then introduced by a versatile no-covalent approach using azido-functionalized dopamine, and alkynyl-terminated RAFT agent was introduced by click chemistry between alkynyl and azido. TBBPA imprinted MIP was finally prepared by RAFT polymerization using 4-vinyl pyridine, ethyleneglycol dimethacrylate, and TBBPA as functional monomer, crosslinker, and template molecule, respectively. Both the morphology and structure of the obtained MIP was characterized. The specific recognition property was measured by adsorption isotherms, adsorption kinetics, selectivity experiments, and competitive binding assay. The results designated that as-prepared MIP exhibited excellent specific recognition properties for TBBPA and it has potential to be used for detection of TBBPA in complicated environment.

2 Experimental

2.1 Materials

Sodium acetate, 2,2-azobisisobutyronitrile (AIBN), and trisodium citrate dihydrate were supplied by the Guangfu

Chemical Industry (Tianjin, China). Ethanol, methanol, dichloromethane (CH_2Cl_2), ethyl acetate, dimethyl sulfoxide (DMSO), ethylene glycol, and acetic acid were supplied by the Guanghua Chemical Industry (Guangdong, China). Sodium azide (NaN_3), toluene, ferric chloride ($FeCl_3$), tetraethyl orthosilicate (TEOS), ammonium hydroxide ($NH_3{\cdot}H_2O$), tetrabutyl titanate (TBOT), and $CuSO_4{\cdot}5H_2O$ were supplied by the Sinopharm Chemical Reagent Co. (Shanghai, China). L-ascorbic acid sodium, 3-bromo-1-propanol, glutaric anhydride, bisphenol A (BPA), N, N'-dicyclohexylcarbodiimide (DCC), 3-hydroxytyramine hydrochloride, ethyleneglycol dimethacrylate (EGDMA), 4,4'-dihydroxybiphenyl (BIP), 4-vinyl pyridine (4-VP), tetrabromobisphenol A (TBBPA), 4-t-butylphenol (BP), and 4-dimethylaminopyridine (DMAP) were provided by Energy Chemical Industry Co. Ltd. (Shanghai, China). Azido-functionalized dopamine is synthesized in keeping with the literature, and the ^{1}H NMR spectrum is presented in Figs. S1–S4 [25, 26].

2.2 Synthesis of Fe_3O_4@SiO_2

Fe_3O_4 was prepared as the method reported in the previous literature [27]. Fe_3O_4@SiO_2 nanospheres were prepared by a typical sol–gel method and detailed procedure list as follows [28]. Fe_3O_4 (0.1 g) nanospheres were dispersed in the mixture of ultrapure water (10 mL), ethanol (30 mL), and 1.2 mL of $NH_3{\cdot}H_2O$. After the ultrasonication was continued for 1 h, 0.2 mL of TEOS was added to the above solution, and the reaction was maintained at 30 ℃ for 4 h. The obtained materials were washed three times with water and ethanol and dried at 60 ℃ under vacuum.

2.3 Preparation of Fe_3O_4@mTiO_2

A uniform mesoporous TiO_2 shell was coated onto Fe_3O_4@SiO_2 according to the method reported previously [29, 30]. The previously prepared Fe_3O_4@SiO_2 (0.2 g) nanoparticles and $NH_3{\cdot}H_2O$ (0.2 mL) were dispersed in ethanol (100 mL) with the aid of ultrasonication for 15 min. Then, 0.75 mL tetrabutyl titanate (TBOT) was added dropwise to the mixture subsequently, and the above system was maintained at 45 °C for 24 h. The obtained nanomaterials were isolated by magnet and washed with water and ethanol, dried under vacuum, and calcined in air at 500 °C for 2 h to form a mesoporous structure.

2.4 Preparation of RAFT agent modified Fe_3O_4@mTiO_2 nanoparticles

Firstly, Fe_3O_4@mTiO_2 (0.1 g) was dispersed in a solution containing azido-functionalized dopamine in CH_2Cl_2. After stirring for 24 h, the azido-functionalized Fe_3O_4@mTiO_2 was obtained after washed with CH_2Cl_2 and dried under vacuum.

Forty milligram of alkynylated 2-dithiobenzoic acid butyrate (CPDB) and 80 mg of Fe_3O_4@mTiO_2-N_3 were dispersed in 25 mL of DMSO. After 15 min of sonication, 3.575 mg of $CuSO_4{\cdot}5H_2O$ and 14.2 mg of sodium ascorbate were separately dissolved in 1 mL water, which was added to the above solution subsequently. The mixture was mechanically stirred at 50 °C for 24 h. The solid product was isolated by magnet and washed several times with water and ethanol and dried under vacuum to obtain Fe_3O_4@mTiO_2-CPDB. The synthesis of alkynylated CPDB and the corresponding ^{1}H NMR spectra (Figure S5) are detailed in the supporting information.

2.5 Preparation of Fe_3O_4@mTiO_2@MIP/NIP

4-VP and EGDMA are used as functional monomers and crosslinkers, respectively. Briefly, 0.21 mL of 4-VP and 136 mg of TBBPA were dissolved in 50 mL of anhydrous toluene and mechanically stirred under N_2 for 10 h. Then, 50 mg of Fe_3O_4@mTiO_2-CPDB was dispersed in the mixture by means of ultrasonic, followed by adding EGDMA (1.189 g) and AIBN (0.02 g), and the reaction was maintained at 60 °C for 24 h under N_2 protection to obtain Fe_3O_4@mTiO_2@MIP. TBBPA was removed using methanol-acetic acid (9:1, v: v) mixed eluent until no TBBPA could be detect by UV–vis spectrophotometer.

The non-imprinted polymer Fe_3O_4@mTiO_2@NIP was prepared in same way without addition of the TBBPA.

2.6 Characterization

Fourier infrared spectrometer (FT-IR, VECTOR-22) was used to obtain the FT-IR spectra of the materials. The microscopic morphology of the sample was observed by transmission electron microscopy (TEM, JEM-2100). The structure of organic species was characterized using nuclear magnetic resonance spectrometer (ADVANCE III 400 MHz). The chemical state of some key element was characterized using an X-ray photoelectron spectroscopy (XPS, AXIS SUPRA). High-performance liquid chromatograph (HPLC-1525) was used to detect the content of TBBPA and its structural analogues in adsorption experiment. The sample injection volume was 10 μL. The mobile phase was composed by methanol and ultrapure water with the ratio of 75:25 (v: v) and the flow rate was 1.0 mL min^{-1}. BPA, BIP, and BP were detected by ultraviolet detector at 278 nm, and TBBPA was detected at 292 nm.

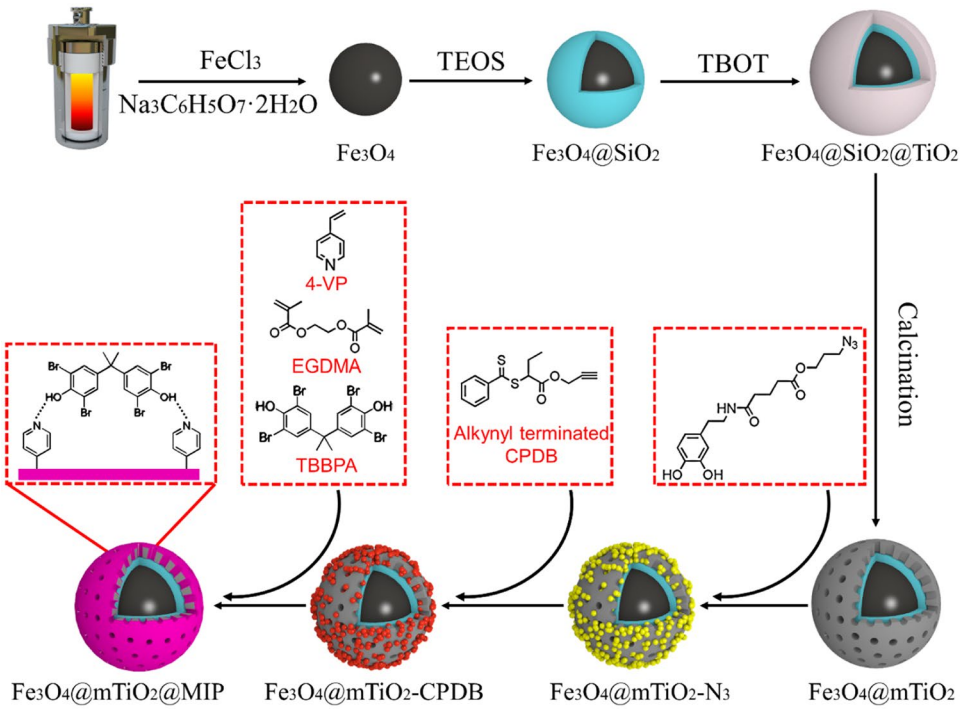

Scheme 1 Schematic illustration of the preparation TBBPA imprinted Fe_3O_4@mTiO$_2$@MIP

2.7 Binding experiments

The binding ability of Fe_3O_4@mTiO$_2$@MIP and Fe_3O_4@mTiO$_2$@NIP for TBBPA was calculated by adsorption experiments. In static adsorption experiments, 10 mg of MIP/NIP nanoparticles was mixed with 10 mL of TBBPA solution in methanol–water (1:1, v: v) in a screw-capped glass tube and sealed and placed in a 30 °C constant temperature shaker for several hours. The concentration of TBBPA varies from 10 to 100 mg L^{-1}. In the kinetic experiments, 10 mg of imprinted or non-imprinted polymer was added to TBBPA solution (10 mL) at a concentration of 10 mg L^{-1} and shaken for different intervals in a 30 °C constant temperature shaker. The MIP/NIP was isolated by magnet, and the resulting supernatant containing TBBPA was measured in HPLC. The adsorption amount of the adsorbent is calculated by the following equation [31–33]:

$$Q_e = \frac{(C_0 - C_t)V}{m} \quad (1)$$

where Q_e (mg g^{-1}) is the equilibrium adsorption amount of TBBPA, V (mL) represents the total volume, C_t (mg L^{-1}) represents the equilibrium concentration of TBBPA, C_o (mg L^{-1}) represents the initial concentration of TBBPA, and m (mg) is the mass of Fe_3O_4@mTiO$_2$@MIP or Fe_3O_4@mTiO$_2$@NIP.

2.8 Selectivity studies

BPA, BIP, and BP were selected as structural analogue to evaluate the selectivity of Fe_3O_4@mTiO$_2$@MIP. 10 mg of Fe_3O_4@mTiO$_2$@MIP and Fe_3O_4@mTiO$_2$@NIP was dispersed in 10 mL of TBBPA and three structural analogues solution with the same concentration (18.5 μmol L^{-1}) using methanol–water (1:1, v: v) as solvent, respectively. The mixture was shaken at 30 °C for 3 h, and the content of TBBPA and its analogues after adsorption was measured using HPLC.

For competitive experiments, TBBPA, BPA, BIP, and BP were dissolved together in a 10 mL of methanol–water mixed solvent (1:1, v: v), and to ensure the same concentration (18.5 μmol L^{-1}) of each substance, 10 mg of Fe_3O_4@mTiO$_2$@MIP was dispersed in the above solution and shaken at 30 °C for 3 h. The content of each component was also measured using HPLC.

3 Results and discussion

3.1 Preparation of the Fe_3O_4@mTiO$_2$@MIP/NIP

The synthesis of MIP is illustrated as Scheme 1. Firstly, monodisperse Fe_3O_4 nanospheres were prepared by solvothermal method. SiO_2 layer was then coated on the surface

of Fe_3O_4 by hydrolysis of TEOS to prevent the leakage and corrosion of Fe_3O_4 nanoparticles. The outer mesoporous TiO_2 layer was prepared by hydrolysis of TBOT, followed by annealing at 500 °C. Azido was then introduced via azido-functionalized dopamine based on a convenient non-covalent effect so that alkynyl-terminated CPDB could be introduced onto the mesoporous support by click chemistry. Finally, the MIP was grafted onto the surface of the support through RAFT polymerization with 4-VP and EGDMA as functional monomer and crosslinker, respectively.

The influence of molar ratio between 4-VP and EGDMA on the imprinting performance was investigated. In general, more functional monomer template complex will be formed as increasing the proportion of the functional monomer. But excessive functional monomer will also produce non-specific binding sites which are generated by the residues of non-assembled functional monomers. Meanwhile, the functional monomers were associated with each other when excessive functional monomers were added, which will decrease the binding sites. The proportion of crosslinker would affect the rigidity of the polymer skeleton and play an important role in the stabilization of the recognition sites. If the crosslinking degree of the as-prepared polymer was low owing to the insufficient dosage of crosslinker, the cavities of the obtained MIP would not be stable and consequently led to the poor binding capacity to target molecule. Figure S6 shows the binding efficiency toward TBBPA of the imprinted and non-imprinted polymers which was prepared with different molar ratio of 4-VP to EGDMA at 1:1, 1:3, and 1:5, respectively. The imprinted factor (IF) was calculated using the following formula [34]:

$$IF = Q_{MIP}/Q_{NIP} \tag{2}$$

where Q_{MIP} and Q_{NIP} correspond to the binding amount of TBBPA by the imprinted and non-imprinted polymer, respectively. Correspondingly, the IF values were 1.71, 2.00, and 1.76. It is clearly seen that the imprinted polymer shows the best binding performance when the ratio of 4-VP to EGDMA is 1:3. Under this condition, the assembly between 4-VP and TBBPA becomes sufficient, and more discerning binding sites which are easily accessible can be obtained with the action of the crosslinker.

3.2 Characterization

Figure 1 shows the TEM morphology of the nanoparticles at each stage of the preparation procedure. Fe_3O_4 nanospheres prepared by solvothermal method exhibit a regular spherical structure of about 200 nm in diameter and exhibit good dispersibility (Fig. 1a, b, c). After SiO_2 was coated on the surface of Fe_3O_4 by a typical sol–gel method, the as-prepared Fe_3O_4@SiO_2 (Fig. 1d, e, f) exhibits smoother surface than Fe_3O_4. The spherical structure of Fe_3O_4 keeps well after SiO_2 coated. The thickness of SiO_2 layer is approximately 60 nm. After TiO_2 layer was further coated, the thickness of shell was increased further, which can be clearly observed in Fig. 1g, h, and i. The obtained TiO_2-coated magnetic nanoparticles are annealed at 500 °C to remove small molecules; a significant change in the roughness of the shell is observed as shown in Fig. 1j, k, and l. This demonstrates the formation of porous structure of TiO_2 shell with thickness of about 22 nm. As shown in Fig. 1m, n, and o and Figure S7, a uniform thin shell layer appears at the surface of the TiO_2 layer after the imprinted polymer was prepared by RAFT polymerization.

The functional groups of the materials that prepared in different stage are investigated by FT-IR, and the spectra are shown in Fig. 2. The absorption peaks at 450 and 570 cm^{-1} in Fig. 2a are ascribed to the vibration of the Fe–O, and the absorption band around 1390 cm^{-1} is caused by the presence of the carboxylate group, which is due to the addition of trisodium citrate in Fe_3O_4 preparation process [2]. After SiO_2 was coated, the new characteristic peak at 1091 cm^{-1} in Fig. 2b indicates the stretching vibration of Si–O-Si. The adsorption band around 805 cm^{-1} is caused by Si–O vibration [35, 36]. Figure 2c is the FT-IR curve of Fe_3O_4@$mTiO_2$. The characteristic absorption occurring in the 400–700 cm^{-1} belongs to the Ti–O-Ti and Ti–O stretching vibration modes [37], which indicated that the TiO_2 layer was formed. After Fe_3O_4@$mTiO_2$ was modified by azido-functionalized dopamine, the new peak around at 2100 cm^{-1} in Fig. 2d can be attributed to the stretching of N = N = N, and conform azido is successfully introduced to the surface of mesoporous support [38]. After click chemistry between azido and alkynyl, the characteristic peak appearing at 1166 cm^{-1} in Fig. 2e corresponds to -C = S, which indicates that the RAFT agent was successfully grafted to the surface of support [39]. In the spectrum of Fe_3O_4@$mTiO_2$@MIP (Fig. 2f), the characteristic peak of C = C stretching from the pyridine ring was detected at 1457 cm^{-1}, which suggested that the imprinted polymer layer was formed on the surface of Fe_3O_4@$mTiO_2$ [40, 41]. The presence of EGDMA can be confirmed by the appearance of stretching vibration adsorption peaks at 1741 cm^{-1} and 1647 cm^{-1} [42, 43].

The crystal structure of the materials at each stage was further characterized by using XRD (Fig. 3). The characteristic diffraction peak in Fig. 3a at $2\theta = 30.0°$, 35.5°, 43.2°, 53.8°, 57.2°, and 62.6° is matched well with Fe_3O_4 nanoparticles [44–46]. The same XRD signal in Fig. 3b indicates that the coating of the SiO_2 layer does not affect the crystal structure of magnetic core. Subsequently, after the TiO_2 layer was coated and calcined at 500 °C, the new characteristic diffraction peaks in Fig. 3c were well-directed to the anatase TiO_2, demonstrating that the emerge of the porous structure of TiO_2 was attributed to the voids between self-aggregated

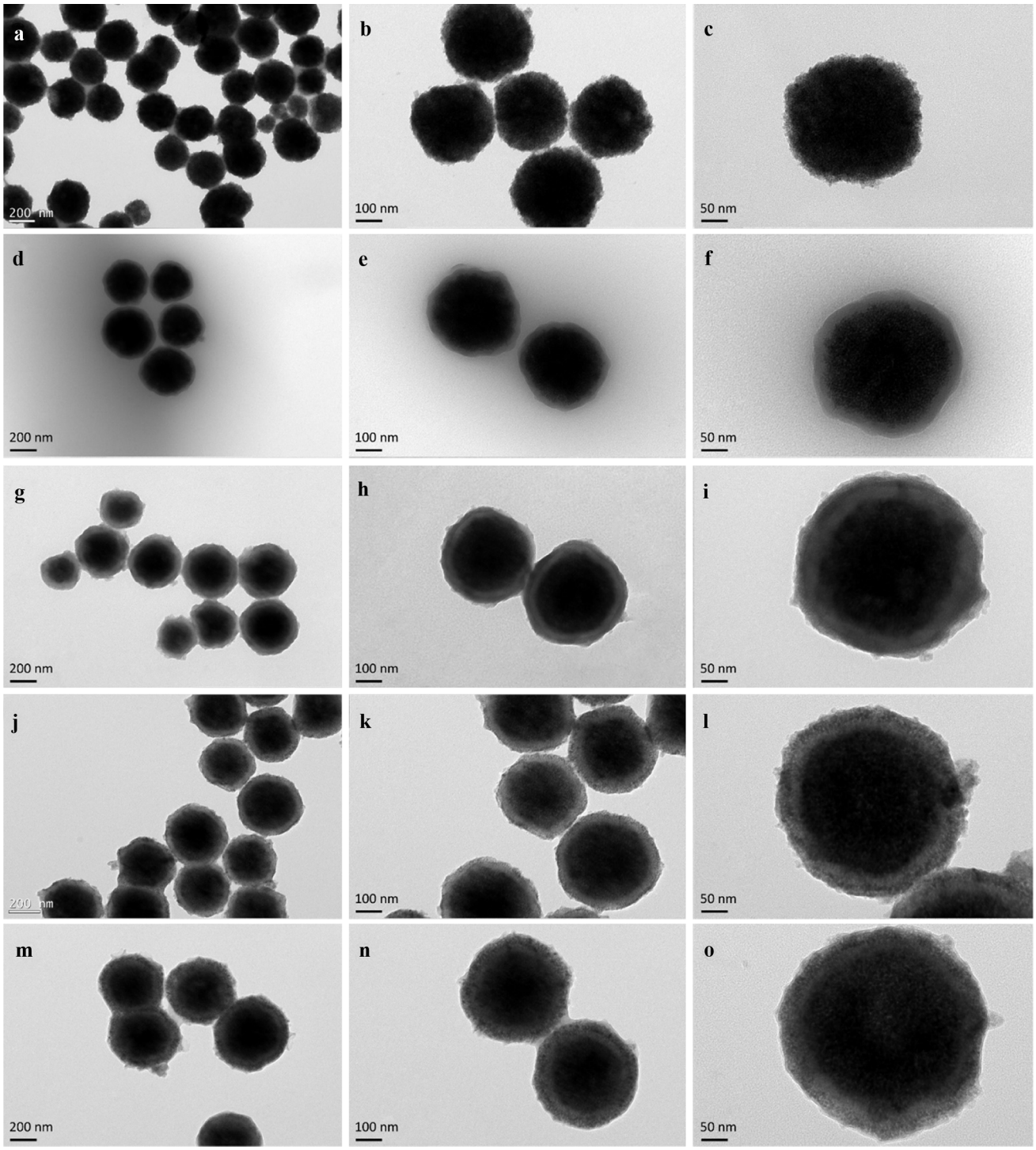

Fig. 1 TEM images of Fe_3O_4 (**a**, **b**, **c**), Fe_3O_4@SiO_2 (**d**, **e**, **f**), Fe_3O_4@TiO_2 (**g**, **h**, **i**), Fe_3O_4@mTiO_2 (**j**, **k**, **l**), and Fe_3O_4@mTiO_2@MIP (**m**, **n**, **o**)

nanocrystals [29, 47–49]. After MIP was prepared, the diffraction peaks of Fe_3O_4@mTiO_2@MIP in Fig. 3d are similar to the peaks of Fe_3O_4@mTiO_2 in Fig. 3c, indicating that the process of polymerization on the surface of TiO_2 does not affect the crystal form of TiO_2[50, 51].

Figure 4 illustrates the magnetic properties of the materials prepared at each stage. The curves a, b, c, and d are hysteresis curves of Fe_3O_4, Fe_3O_4@SiO_2, Fe_3O_4@mTiO_2, and Fe_3O_4@mTiO_2@MIP, respectively. As the experiment progressed, the decrease of specific saturation magnetizations was caused

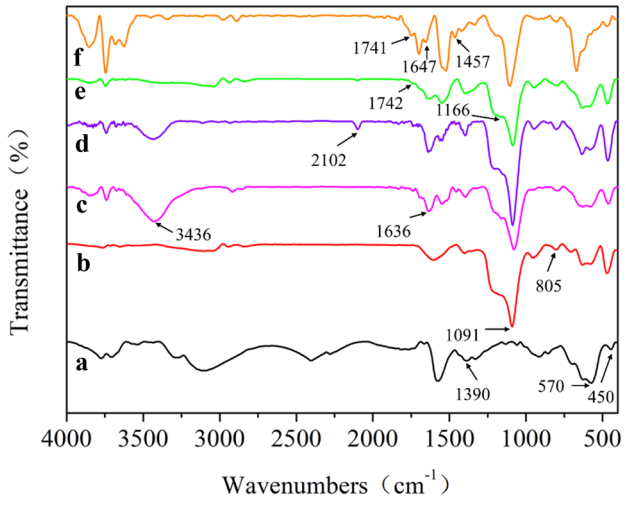

Fig. 2 FT-IR spectra of Fe_3O_4 (**a**), Fe_3O_4@SiO_2 (**b**), Fe_3O_4@$mTiO_2$ (**c**), Fe_3O_4@$mTiO_2$-N_3 (**d**), Fe_3O_4@$mTiO_2$-CPDB (**e**), and Fe_3O_4@$mTiO_2$@MIP (**f**)

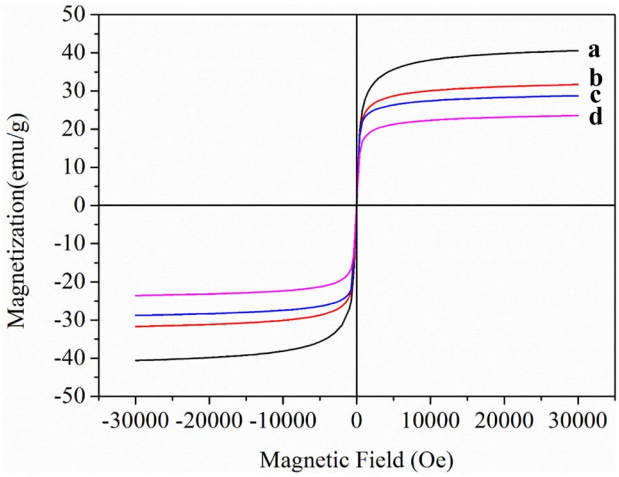

Fig. 4 VSM curves of Fe_3O_4 (**a**), Fe_3O_4@SiO_2 (**b**), Fe_3O_4@$mTiO_2$ (**c**), and Fe_3O_4@$mTiO_2$@MIP (**d**)

by the encapsulation of SiO_2, TiO_2, and MIP layer. But the saturation magnetization of Fe_3O_4@$mTiO_2$@MIP is still 23 emu/g, which ensure that it could be quickly and completely separated by the aid of a magnet. At the same time, it can be seen that all of the samples exhibit superparamagnetic behavior because the coercivity and remanence of the sample are not detected [17, 52]. Sensitive magnetic response is important for the later application of these samples.

The composition of the nanoparticles were further characterized by XPS. The signal located at 457 eV can be attributed to Ti 2p in the wide scan spectra of Fe_3O_4@$mTiO_2$ (Fig. 5Aa) [53]. In Fig. 5Ab, the N 1 s peak appears at

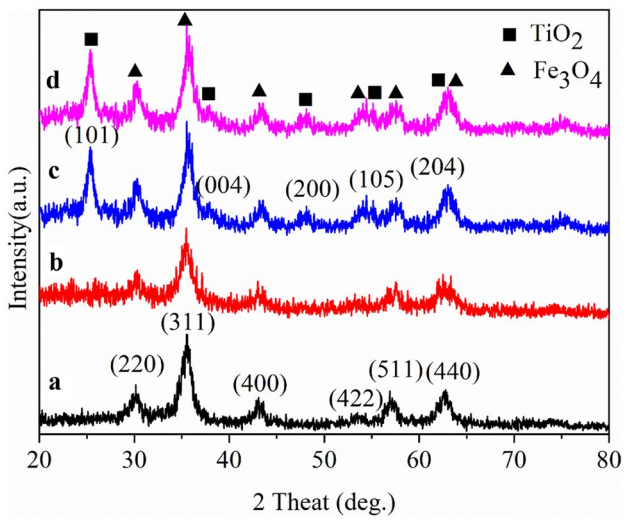

Fig. 3 XRD patterns of Fe_3O_4 (**a**), Fe_3O_4@SiO_2 (**b**), Fe_3O_4@$mTiO_2$ (**c**), and Fe_3O_4@$mTiO_2$@MIP (**d**)

398.5 eV in the wide scan spectra of Fe_3O_4@$mTiO_2$-N_3, suggesting that the azido was introduced on the surface of Fe_3O_4@$mTiO_2$ by azido-functionalized dopamine successfully [54]. The S 2p peak at 164 eV in Fe_3O_4@$mTiO_2$-CPDB indicating CPDB was successfully grafted onto the Fe_3O_4@$mTiO_2$ (Fig. 5Ac) [55].

In the high-resolution spectrum of Ti in Fe_3O_4@$mTiO_2$ (Fig. 5B), two peaks appeared at 458.3 eV and 464.1 eV can be attributed to $Ti2p_{3/2}$ and $Ti2p_{1/2}$, indicating that mesoporous TiO_2 shell was successfully formed [53, 56–58]. In the high-resolution spectrum of the N element in Fe_3O_4@$mTiO_2$-N_3 (Fig. 5C), the singles at 398.6, 399.8, and 402.2 eV correspond to C-N, -N–H, and -N=, respectively [28, 59, 60]. It was proved that the azido functional dopamine was effectively grafted on the surface of TiO_2. In the spectrum of S2p in Fe_3O_4@$mTiO_2$-CPDB (Fig. 5D), the appearance of C=S (160.9 eV) and C-S-C (164.5 eV) peaks indicates that CPDB was successfully grafted onto the Fe_3O_4@$mTiO_2$ by click chemistry [55]. By fitting the C 1 s spectra of Fe_3O_4@$mTiO_2$@MIP curve (Fig. 5E), four peaks at the binding energy of 284.6, 286.0, 286.6, and 288.6 eV were caused by the presence of C=C/C–C/C-H, C-N/C=S, C=N/C-O/C-S, and C=O, respectively. The content of C=C/C–C/C-H, C-N/C=S, C=N/C-O/C-S, and C=O is 80.6%, 14.3%, 3.7%, and 1.4%, respectively [61]. In the high-resolution spectrum of the O element in Fe_3O_4@$mTiO_2$@MIP in Fig. 5F, the peaks at 530 eV and 532.5 eV correspond to the O=C and O-C, respectively [62]. The overall analysis of the XPS spectrum fully confirmed that the imprinted polymer layer was well-formed on the surface of the Fe_3O_4@$mTiO_2$ by RAFT polymerization.

The specific surface area and porosity of Fe_3O_4@$mTiO_2$ were evaluated by N_2 adsorption–desorption isotherms. As shown in Fig. 6a, the isotherms of Fe_3O_4@$mTiO_2$ exhibit a

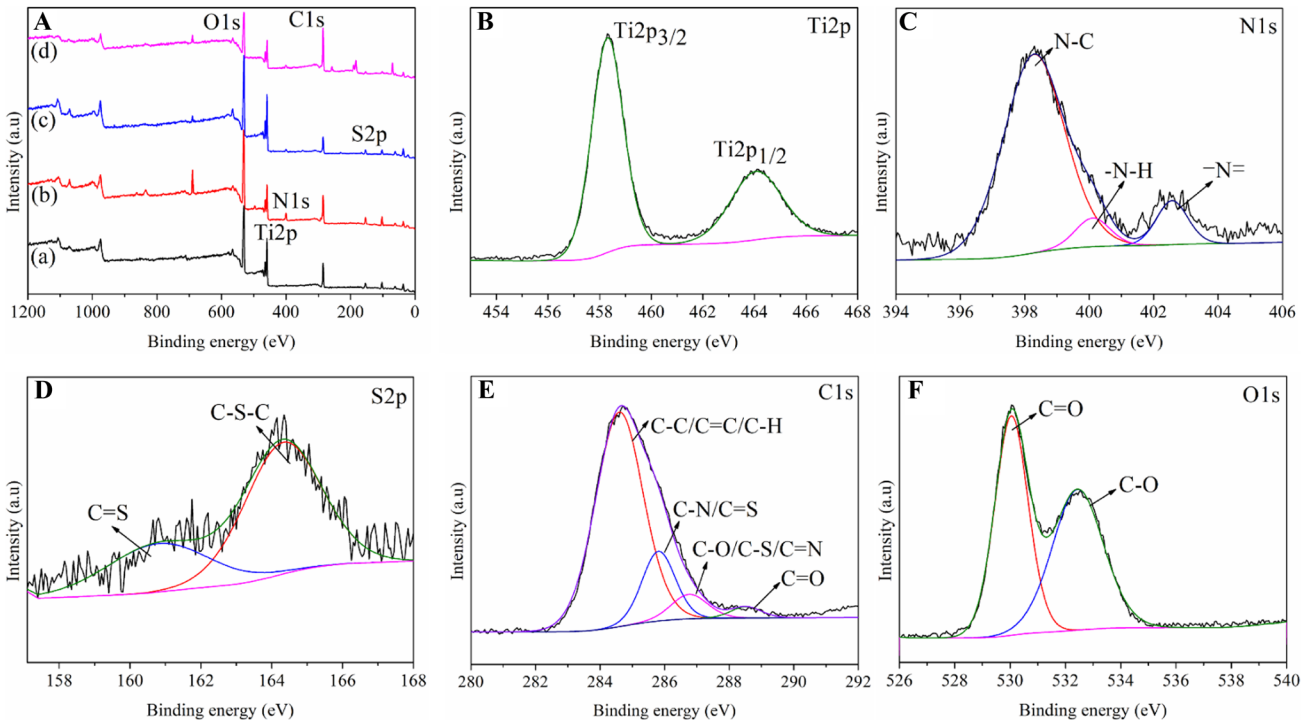

Fig. 5 (**A**) XPS wide scan spectrum of Fe_3O_4@$mTiO_2$ (**a**), Fe_3O_4@$mTiO_2$-N_3 (**b**), Fe_3O_4@$mTiO_2$-CPDB (**c**), Fe_3O_4@$mTiO_2$@MIP (**d**), and high-resolution spectrum of Ti 2p in Fe_3O_4@$mTiO_2$ (**B**), N 1 s in Fe_3O_4@$mTiO_2$-N_3 (**C**), S 2p in Fe_3O_4@$mTiO_2$-CPDB (**D**), C 1 s and O 1 s in Fe_3O_4@$mTiO_2$@MIP (**E, F**).

typical type IV isotherm, and the specific surface area of the Fe_3O_4@$mTiO_2$ obtained by Brunauer–Emmett–Teller analysis is 69.818 $m^2\ g^{-1}$. At $P/P_0 = 0.05–0.35$, a gentle increase in the amount of adsorption indicates that the N_2 was adsorbed on the inner surface of the mesopores in a single layer to a plurality of layers. When P/P_0 is between 0.40 and 0.80, the sudden increase in the amount of adsorption reflects the size of the sample pore size. At the higher relative pressure stage, the desorption isotherm does not coincide with the adsorption isotherm, and the desorption isotherm is above the adsorption isotherm, indicating an H_3 hysteresis loop depending on the type of hysteresis loop [63]. This feature of the material will be better defined for the identification of the template and provides a higher binding capacity. Figure 6b shows the pore size distribution curve; the average pore diameter of the material obtained according to the Barrett-Joyner-Halenda pore size distribution curve was 4.626 nm, indicating the presence of mesopores structure in the matrix.

3.3 Absorption kinetics of Fe_3O_4@$mTiO_2$@MIP

As shown in the adsorption kinetic curve in Fig. 7a, the adsorption capacities of Fe_3O_4@$mTiO_2$@MIP and Fe_3O_4@$mTiO_2$@NIP increased with time, and the adsorption capacity reached equilibrium after 20 min. Compared to the equilibrium time of TBBPA imprinted polymer that prepared

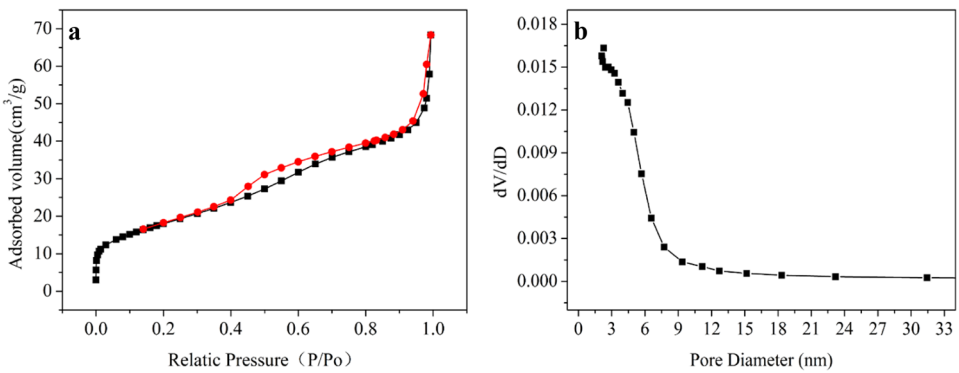

Fig. 6 N_2 adsorption–desorption isotherms (**a**) and pore size distribution (**b**) of the Fe_3O_4@$mTiO_2$ nanocomposites

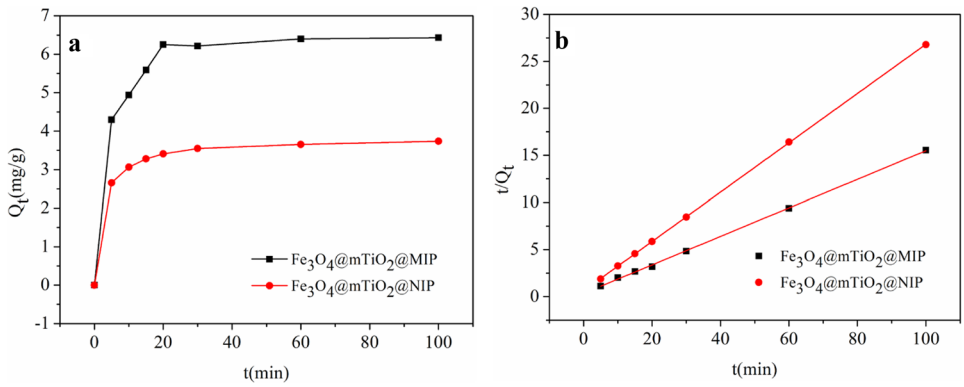

Fig. 7 Kinetic adsorption curves (**a**) of Fe_3O_4@mTiO_2@MIP and Fe_3O_4@mTiO_2@NIP for TBBPA and pseudo-second-order kinetic model fitting curve (**b**)

by traditional free radical polymerization method [4], the equilibrium time in this work only takes 20 min, which is dramatically shorter than the reported valve of 40 min. This phenomenon is mainly thanks to the controllability of RAFT polymerization; the thin imprinted layer makes the imprinted sites more accessible to TBBPA and exhibits faster binding capabilities. It is clearly shown in Fig. 7a that the binding amount of Fe_3O_4@mTiO_2@MIP is higher than that of Fe_3O_4@mTiO_2@NIP due to the specific imprinted site generated on the surface for specific recognition of TBBPA.

The adsorption mechanism of the imprinted polymer was explained by using the following pseudo-first-order and pseudo-second-order kinetics models; the equations of them are depicted in following Eqs. (3–4), respectively [64, 65]:

$$\log\left(Q_e - Q_t\right) = \log Q_e - \frac{k_1}{2.303}t \tag{3}$$

$$\frac{t}{Q_t} = \frac{1}{k_2 Q_e^2} + \frac{t}{Q_e} \tag{4}$$

wherein Q_t and Q_e represent the adsorption amount at t and equilibrium, t represents the adsorption time, and k_1 and k_2 represent the pseudo-first-order rate constant and the pseudo-second-order rate constant, respectively.

From the fitting curve of pseudo-second-order kinetic model in Fig. 7b and the relevant parameters that listed in the Table 1, it is suggested that the pseudo-second-order adsorption kinetics model agreed better with the adsorption process of TBBPA by MIP/NIP and the correlation coefficient of MIP was 0.999. At the same time, the experimental $Q_{e,\,exp}$ is closer to the theoretically calculated $Q_{e,\,cal}$. This indicates that chemisorption controls the adsorption of TBBPA by Fe_3O_4@SiO_2@mTiO_2@MIP, and TBBPA binds to the identification site in the imprinted polymer layer by a non-covalent bond [66].

3.4 Adsorption isotherms of Fe_3O_4@mTiO_2@MIP

The static adsorption experiment was also conducted to further understand the adsorption capability of Fe_3O_4@mTiO_2@MIP and Fe_3O_4@mTiO_2@NIP. As shown in the adsorption isotherms in Fig. 8a, the adsorption amount of Fe_3O_4@mTiO_2@MIP and Fe_3O_4@mTiO_2@NIP increases as the solution concentration of TBBPA increases and reaches a state of adsorption saturation after a certain time. However, the adsorption amount of Fe_3O_4@mTiO_2@MIP was significantly greater than that of Fe_3O_4@mTiO_2@NIP, indicating the higher specific binding ability of Fe_3O_4@mTiO_2@MIP to the template molecule, since the imprinted sites existed on the material surface. The adsorption capacity of the imprinted polymer for TBBPA that prepared on the non-porous carrier was also studied. As can be seen from Fig. 8a, both the Fe_3O_4@TiO_2@MIP and Fe_3O_4@TiO_2@NIP exhibit weaker adsorption capacity towards TBBPA than Fe_3O_4@mTiO_2@MIP/NIP, respectively. The Q_{max} of the imprinted polymer prepared (41.67 mg g^{-1}) on the mesoporous support was 1.6 times higher than that prepared on non-porous support (25.64 mg g^{-1}). The porous structure of the support can provide more binding site and make recognition sites more accessible for TBBPA [21]. The experiment results further

Table.1 The kinetic model parameters for adsorption of TBBPA by Fe_3O_4@mTiO_2@MIP and Fe_3O_4@mTiO_2@NIP

Samples	Pseudo-first-order				Pseudo-second-order		
	$Q_{e,\,exp}$ (mg g^{-1})	$Q_{e,\,cal}$ (mg g^{-1})	k_1 (min^{-1})	R^2	$Q_{e,\,cal}$ (mg g^{-1})	k_2 (g $mg^{-1}min^{-1}$)	R^2
MIP	6.43	2.154	0.074	0.865	6.60	0.065	0.999
NIP	3.73	0.981	0.045	0.915	3.82	0.109	0.999

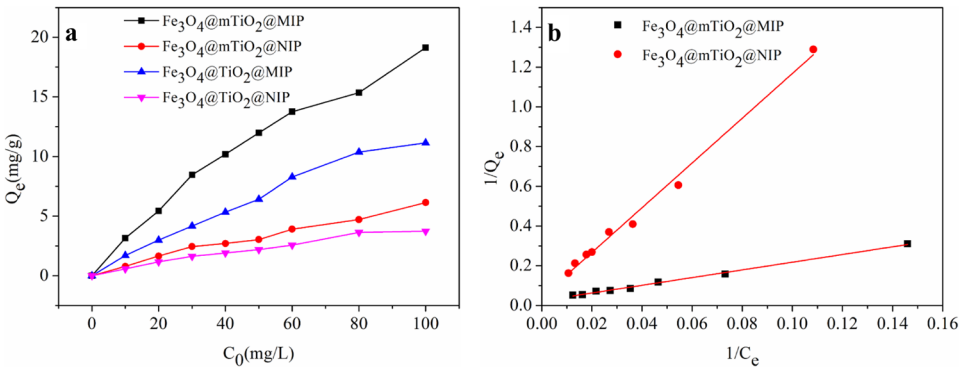

Fig. 8 Fe_3O_4@TiO$_2$@MIP/NIP and Fe_3O_4@mTiO$_2$@MIP/NIP adsorption isotherms (**a**) for TBBPA and Langmuir isotherm adsorption model fitting curve of Fe_3O_4@mTiO$_2$@MIP/NIP (**b**)

confirmed that mesoporous structure of support exhibits more advantages than non-porous support as the imprinted polymer carrier.

The adsorption mechanism of Fe_3O_4@mTiO$_2$@MIP/NIP was determined according to two different adsorption isotherms of Langmuir and Freundlich; the equations for the two models are as follows [64]:

$$\frac{C_e}{Q_e} = \frac{1}{Q_m K_l} + \frac{C_e}{Q_m} \tag{5}$$

$$\ln Q_e = \ln K_F + \frac{1}{n}\ln C_e \tag{6}$$

Among them, Q_m represents the maximum adsorption capacity of the imprinted material, Q_e represents the adsorption capacity at the time of adsorption equilibrium, and C_e is the concentration of TBBPA at equilibrium. K_l is the adsorption equilibrium constant, and n and K_F represent the adsorption strength and relative adsorption capacity, respectively.

The Langmuir isotherm adsorption model fitting curve in Fig. 8b and the data list in Table 2 clearly show that the adsorption process matches well with Langmuir isotherm equation, and the correlation coefficient of MIP is 0.995. The results indicate that the Langmuir isotherm equation is more appropriate for defining the adsorption of TBBPA. Therefore, it can be considered that TBBPA is adsorbed on the surface of the Fe_3O_4@mTiO$_2$@MIP in the form of a monomolecular layer [67]. The Q_m of Fe_3O_4@mTiO$_2$@MIP for TBBPA was 41.67 mg g^{-1} and was higher than the value reported in literature [5, 68]. This is mainly due to the advantages generated by RAFT polymerization and mesoporous structure of the outer shell which can provide more binding sites to effectively improve the binding capacity [21].

3.5 Selectivity of Fe_3O_4@mTiO$_2$@MIP nanoparticles

Excellent selectivity for TBBPA is crucial for the as-prepared Fe_3O_4@mTiO$_2$@MIP. Therefore, some compounds (BPA, BIP, and BP) with similar structures to TBBPA were selected for comparative experiments. Their chemical structures are shown in the Fig. 9.

The same amount of Fe_3O_4@mTiO$_2$@MIP and Fe_3O_4@mTiO$_2$@NIP was separately dispersed in the solutions of TBBPA, BPA, BP, and BIP with the same concentrations, and the removal efficiency of imprinted and non-imprinted polymer for TBBPA and its structural analogues was examined. It is found from the results in Fig. 10 that the removal efficiency of Fe_3O_4@mTiO$_2$@MIP for TBBPA is significantly higher than that of the other three substances, which proves the specific recognition property of the imprinted material for TBBPA. This is mainly caused by the specific recognition cavity exist at the surface of Fe_3O_4@mTiO$_2$@MIP, which is completely corresponding to the shape, size, and spatial organization of TBBPA, while BIP, BP, and BPA are not complementary to the recognition site, and the removal efficiency is lower. The above results further demonstrate that Fe_3O_4@mTiO$_2$@MIP can be used to selectively detect TBBPA.

In addition, competitive binding experiments were implemented to verify the specific binding property of Fe_3O_4@mTiO$_2$@MIP to TBPPA. A mixed solution (10 mL) with the equimolar concentrations (18.5 μmol

Table 2 Fe_3O_4@mTiO$_2$@MIP and Fe_3O_4@mTiO$_2$@NIP isothermal adsorption model parameters for TBBPA

Samples	Langmuir			Freundlich		
	Qm (mg g^{-1})	*KL* (L mg^{-1})	R^2	*KF* ((mg g^{-1}) (L mg^{-1})1/n)	*1/n*	R^2
MIP	41.67	0.008	0.995	0.77	0.779	0.988
NIP	20.92	0.004	0.992	0.397	0.849	0.983

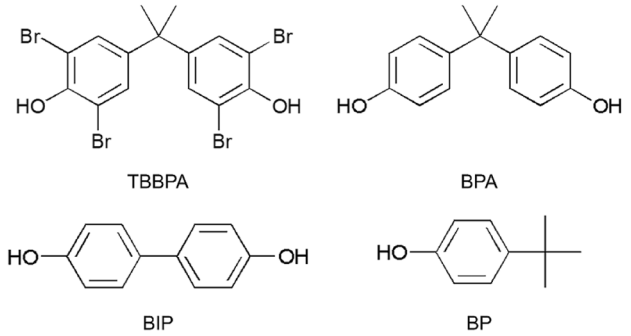

Fig. 9 The structural formula of TBBPA, BPA, BIP, and BP

L^{-1}) of TBBPA, BPA, BIP, and BP was prepared, and then 10 mg of Fe_3O_4@mTiO_2@MIP was added. As shown in Figure S8, the Fe_3O_4@mTiO_2@MIP presents the highest removal efficiency for TBBPA. Conversely, the removal efficiency for the other three substances was very low. This indicates that the imprinted polymer is capable of specifically recognizing TBBPA in a complex environment.

3.6 Reusability of Fe_3O_4@mTiO_2@MIP

Reusability is critical for the practical application of imprinted materials. The recyclability of the imprinted material was detected by performing adsorption–desorption-resorption of the imprinted material. Figure 11 shows the adsorption effect of the imprinted material on TBBPA during 5 cycles. It was

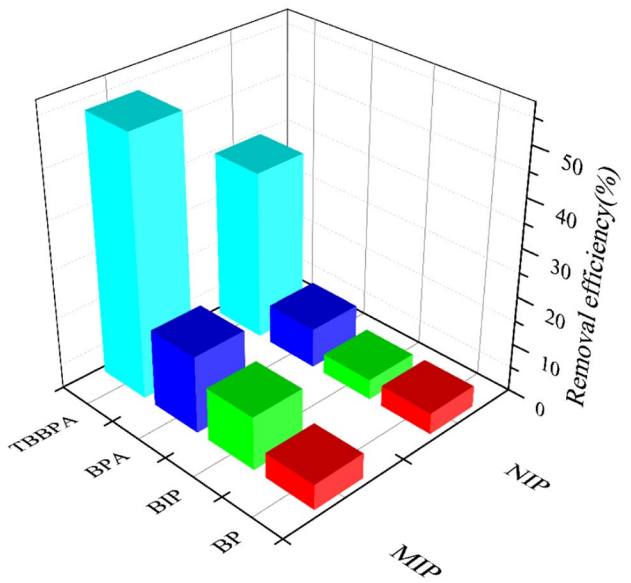

Fig. 10 Adsorption properties of Fe_3O_4@mTiO_2@MIP and Fe_3O_4@mTiO_2@NIP for TBBPA and its structural analogs

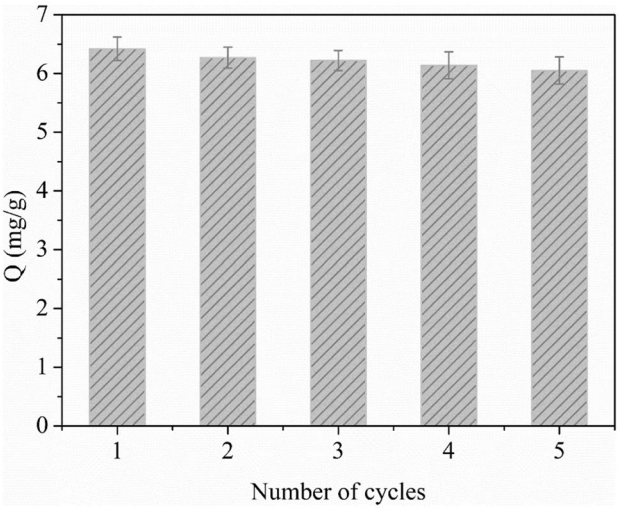

Fig. 11 Reusability of Fe_3O_4@mTiO_2@MIP

observed that it still maintains a high adsorption amount without significant decrease and indicates the imprinted material has excellent stability.

4 Conclusions

Magnetic surface molecularly imprinted polymer was prepared using magnetic mesoporous Fe_3O_4@mTiO_2 nanoparticles as support by RAFT polymerization and was used for rapid detection of TBBPA. The prepared imprinted material has excellent specific binding properties for TBBPA in short time. In addition, the presence of the magnetic core facilitates the rapid separation of the imprinted material. The combination of RAFT polymerization and mesoporous structure of outer TiO_2 layer makes more effective recognition site existence which can affect specific binding properties of obtained imprinted polymer effectively. In practical applications, satisfactory selection performance and recyclable results indicate a promising separation of TBBPA in complex environments.

Supplementary information The online version contains supplementary material available at https://doi.org/10.1007/s42114-021-00361-7.

Funding The authors would like to express their gratitude for research funding provided by the National Natural Science Foundation of China (Program No. 21806097, 21978164, 22078189), the Industrialization Project of Shaanxi Education Department (Program No. 19JC010), the Scientific Research Program Funded by Shaanxi Provincial Education Department (Program No. 18JK0104), and the Research Starting Foundation of Shaanxi University of Science and Technology (Program No. 2016BJ-80).

Declarations

Conflict of interest The authors declare no competing interests.

References

1. Shen W, Xu G, Wei F, Yang J, Cai Z, Hu Q (2013) Preparation and application of imprinted polymer for tetrabromobisphenol A using tetrachlorobisphenol A as the dummy template. Anal Methods 5(19):5208–5214
2. Shao Y, Zhou L, Wu Q, Bao C, Liu M (2017) Preparation of novel magnetic molecular imprinted polymers nanospheres via reversible addition - fragmentation chain transfer polymerization for selective and efficient determination of tetrabromobisphenol A. J Hazard Mater 339:418–426
3. Zhang Z, Cai R, Long F, Wang J (2015) Development and application of tetrabromobisphenol A imprinted electrochemical sensor based on graphene/carbon nanotubes three-dimensional nanocomposites modified carbon electrode. Talanta 134:435–442
4. Wu Q, Li M, Huang Z, Shao Y, Bai L, Zhou L (2018) Well-defined nanostructured core-shell magnetic surface imprinted polymers (Fe_3O_4@SiO_2@MIPs) for effective extraction of trace tetrabromobisphenol A from water. J Ind Eng Chem 60:268–278
5. Yin YM, Chen YP, Wang XF, Liu Y, Liu HL, Xie MX (2012) Dummy molecularly imprinted polymers on silica particles for selective solid-phase extraction of tetrabromobisphenol A from water samples. J Chromatogr A 1220:7–13
6. Polo M, Gómez-Noya G, Quintana JB, Llompart M, García-Jares C, Cela R (2004) Development of a solid-phase microextraction gas chromatography/tandem mass spectrometry method for polybrominated diphenyl ethers and polybrominated biphenyls in water samples. Anal Chem 76(4):1054–1062
7. ten Dam G, Pardo O, Traag W, van der Lee M, Peters R (2012) Simultaneous extraction and determination of HBCD isomers and TBBPA by ASE and LC-MSMS in fish. J Chromatogr B 898:101–110
8. Chen L, Wang X, Lu W, Wu X, Li J (2016) Molecular imprinting: perspectives and applications. Chem Soc Rev 45(8):2137–2211
9. Liu G, Chen Z, Jiang X, Feng D-Q, Zhao J, Fan D, Wang W (2016) In-situ hydrothermal synthesis of molecularly imprinted polymers coated carbon dots for fluorescent detection of bisphenol A. Sens Actuators, B 228:302–307
10. Hou J, Li H, Wang L, Zhang P, Zhou T, Ding H, Ding L (2016) Rapid microwave-assisted synthesis of molecularly imprinted polymers on carbon quantum dots for fluorescent sensing of tetracycline in milk. Talanta 146:34–40
11. Dirion B, Cobb Z, Schillinger E, Andersson LI, Sellergren B (2003) Water-compatible molecularly imprinted polymers obtained via high-throughput synthesis and experimental design. J Am Chem Soc 125(49):15101–15109
12. Chen YP, Wang DN, Yin YM, Wang LY, Wang XF, Xie MX (2012) Quantum dots capped with dummy molecularly imprinted film as luminescent sensor for the determination of tetrabromobisphenol A in water and soils. J Agric Food Chem 60(42):10472–10479
13. Yu J, Wang X, Kang Q, Li J, Shen D, Chen L (2017) One-pot synthesis of a quantum dot-based molecular imprinting nanosensor for highly selective and sensitive fluorescence detection of 4-nitrophenol in environmental waters. Environ Sci: Nano 4(2):493–502
14. Zhang Z, Li J, Wang X, Shen D, Chen L (2015) Quantum dots based mesoporous structured imprinting microspheres for the sensitive fluorescent detection of phycocyanin. ACS Appl Mater Interfaces 7(17):9118–9127
15. Qin L, He XW, Zhang W, Li WY, Zhang YK (2009) Surface-modified polystyrene beads as photografting imprinted polymer matrix for chromatographic separation of proteins. J Chromatogr A 1216(5):807–814
16. Li Y, Li X, Chu J, Dong C, Qi J, Yuan Y (2010) Synthesis of core-shell magnetic molecular imprinted polymer by the surface RAFT polymerization for the fast and selective removal of endocrine disrupting chemicals from aqueous solutions. Environ Pollut 158(6):2317–2323
17. Yuan B, Li L, Murugadoss V, Vupputuri S, Wang J, Alikhani N, Guo Z (2020) Nanocellulose-based composite materials for wastewater treatment and waste-oil remediation. ES Food Agrofor 1:41–52
18. Wang X, Mao H, Huang W, Guan W, Zou X, Pan J, Yan Y (2011) Preparation of magnetic imprinted polymer particles via microwave heating initiated polymerization for selective enrichment of 2-amino-4-nitrophenol from aqueous solution. Chem Eng J 178:85–92
19. Hu X, Xie L, Guo J, Li H, Jiang X, Zhang Y, Shi S (2015) Hydrophilic gallic acid-imprinted polymers over magnetic mesoporous silica microspheres with excellent molecular recognition ability in aqueous fruit juices. Food Chem 179:206–212
20. Qian K, Fang G, Wang S (2011) A novel core-shell molecularly imprinted polymer based on metal-organic frameworks as a matrix. Chem Commun 47(36):10118–10120
21. Xie L, Guo J, Zhang Y, Hu Y, You Q, Shi S (2015) Novel molecular imprinted polymers over magnetic mesoporous silica microspheres for selective and efficient determination of protocatechuic acid in Syzygium aromaticum. Food Chem 178:18–25
22. Li Y, Li X, Dong C, Li Y, Jin P, Qi J (2009) Selective recognition and removal of chlorophenols from aqueous solution using molecularly imprinted polymer prepared by reversible addition-fragmentation chain transfer polymerization. Biosens Bioelectron 25(2):306–312
23. Pan G, Zhang Y, Ma Y, Li C, Zhang H (2011) Efficient one-pot synthesis of water-compatible molecularly imprinted polymer microspheres by facile RAFT precipitation polymerization. Angew Chem Int Ed 50(49):11731–11734
24. Zhao M, Chen X, Zhang H, Yan H, Zhang H (2014) Well-defined hydrophilic molecularly imprinted polymer microspheres for efficient molecular recognition in real biological samples by facile RAFT coupling chemistry. Biomacromol 15(5):1663–1675
25. Watson MA, Lyskawa J, Zobrist C, Fournier D, Jimenez M, Traisnel M, Gengembre L, Woisel P (2010) A "clickable" titanium surface platform. Langmuir 26(20):15920–15924
26. Chan EWC, Baek P, Barker D, Travas-Sejdic J (2015) Highly functionalisable polythiophene phenylenes Polym Chem 6(43):7618–7629
27. Deng Y, Cai Y, Sun Z, Liu J, Liu C, Wei J, Li W, Liu C, Wang Y, Zhao D (2010) Multifunctional mesoporous composite microspheres with well-designed nanostructure: a highly integrated catalyst system. J Am Chem Soc 132(24):8466–8473
28. Li D, Yi R, Tian J, Li J, Yu B, Qi J (2017) Rational synthesis of hierarchical magnetic mesoporous silica microspheres with tunable mesochannels for enhanced enzyme immobilization. Chem Commun 53(63):8902–8905
29. Li W, Yang J, Wu Z, Wang J, Li B, Feng S, Deng Y, Zhang F, Zhao D (2012) A versatile kinetics-controlled coating method to construct uniform porous TiO_2 shells for multifunctional core-shell structures. J Am Chem Soc 134(29):11864–11867
30. Gu Y, Pan Z, Zhang H, Zhu J, Yuan B, Pan D, Wu C, Dong B, Guo Z (2020) Synthesis of high performance diesel oxidation catalyst using novel mesoporous AlLaZrTiOx mixed oxides by a modified sol-gel method. Adv Compos Hybrid Mater 3(4):583–593
31. Chen J, Wang X, Huang Y, Lv S, Cao X, Yun J, Cao D (2018) Adsorption removal of pollutant dyes in wastewater by nitrogen-doped porous carbons derived from natural leaves. Eng Sci 5:30–38
32. Elazzouzi M, Haboubi K, Elyoubi MS, Kasmi AE (2019) A developed low-cost electrocoagulation process for efficient phosphate and COD removals from real urban wastewater. ES Energy Environ 5:66–74
33. Lin C, Qiao Z, Zhang J, Tang J, Zhang Z, Guo Z (2019) Highly efficient fluoride adsorption in domestic water with RGO/Ag nanomaterials. ES Energy Environ 4:27–33

34. He Y, Huang Y, Jin Y, Liu X, Liu G, Zhao R (2014) Well-defined nanostructured surface-imprinted polymers for highly selective magnetic separation of fluoroquinolones in human urine. ACS Appl Mater Interfaces 6(12):9634–9642
35. Zhu Q, Wang B, Tan T (2016) Conversion of ethanol and acetaldehyde to butadiene over MgO-SiO_2 catalysts: effect of reaction parameters and interaction between MgO and SiO_2 on catalytic performance. ACS Sustainable Chem Eng 5(1):722–733
36. Ma H, Shi J, Zhu X, Zhang Z, Li J, Cao S (2019) AuNRs/mesoporous silica/hydroxyapatite nanovehicles with thermally responsive polymeric cap for remotely controlled drug delivery. Adv Compos Hybrid Mater 2(2):242–253
37. Zhao T, Xing Z, Xiu Z, Li Z, Yang S, Zhu Q, Zhou W (2019) Surface defect and rational design of TiO_{2-x} nanobelts/ g-C_3N_4 nanosheets/ CdS quantum dots hierarchical structure for enhanced visible-light-driven photocatalysis. Int J Hydrogen Energy 44(3):1586–1596
38. Barras A, Lyskawa J, Szunerits S, Woisel P, Boukherroub R (2011) Direct functionalization of nanodiamond particles using dopamine derivatives. Langmuir 27(20):12451–12457
39. Chang L, Li Y, Chu J, Qi J, Li X (2010) Preparation of core-shell molecularly imprinted polymer via the combination of reversible addition-fragmentation chain transfer polymerization and click reaction. Anal Chim Acta 680(1–2):65–71
40. Zhao L, Zhao F, Zeng B (2014) Synthesis of water-compatible surface-imprinted polymer via click chemistry and RAFT precipitation polymerization for highly selective and sensitive electrochemical assay of fenitrothion. Biosens Bioelectron 62:19–24
41. Guo J, Li X, Liu H, Young DP, Song G, Song K, Zhu J, Kong J, Guo Z (2021) Tunable magnetoresistance of core-shell structured polyaniline nanocomposites with 0-, 1-, and 2-dimensional nanocarbons. Adv Compos Hybrid Mater 4(1):51–64
42. Fei G, Wang Y, Wang H, Ma Y, Guo Q, Huang W, Yang D, Shao Y, Ni Y (2019) Fabrication of bacterial cellulose/polyaniline nanocomposite paper with excellent conductivity, strength, and flexibility. ACS Sustainable Chem Eng 7(9):8215–8225
43. Lu X, Yang Y, Zeng Y, Li L, Wu X (2018) Rapid and reliable determination of p-nitroaniline in wastewater by molecularly imprinted fluorescent polymeric ionic liquid microspheres. Biosens Bioelectron 99:47–55
44. Zhou G, Wang D-W, Li F, Zhang L, Li N, Wu Z-S, Wen L, Lu GQ, Cheng H-M (2010) Graphene-wrapped Fe_3O_4 anode material with improved reversible capacity and cyclic stability for lithium ion batteries. Chem Mater 22(18):5306–5313
45. Guo J, Chen Z, Abdul W, Kong J, Khan MA, Young DP, Zhu J, Guo Z (2021) Tunable positive magnetoresistance of magnetic polyaniline nanocomposites. Adv Compos Hybrid Mater. https://doi.org/10.1007/s42114-021-00242-z
46. Chandane P, Jadhav U (2021) A simple colorimetric detection of malathion using peroxidase like activity of Fe_3O_4 magnetic nanoparticles. ES Food Agrofor 3:31–36
47. Danish M, Qamar M, Suliman MH, Muneer M (2020) Photoelectrochemical and photocatalytic properties of Fe@ZnSQDs/TiO_2 nanocomposites for degradation of different chromophoric organic pollutants in aqueous suspension. Adv Compos Hybrid Mater 3(4):570–582
48. Singh N, Jana S, Singh GP, Dey RK (2020) Graphene-supported TiO_2: study of promotion of charge carrier in photocatalytic water splitting and methylene blue dye degradation. Adv Compos Hybrid Mater 3(1):127–140
49. Bhalekar VP, Baviskar PK, Prasad R, Palve BM, Kadam VS, Pathan HM (2019) PbS sensitized TiO_2 based quantum dot solar cells with efficiency greater than 5% under artificial light: effect of compact layer and surface passivation. Eng Sci 7:38–42
50. Mahadik SA, Patil A, Pathan HM, Salunke-Gawali S, Butcher RJ (2020) Thionaphthoquinones as photosensitizers for TiO_2 nanorods and ZnO nanograin based dye-sensitized solar cells: effect of nanostructures on charge transport and photovoltaic performance. Eng Sci 14:46–58
51. Patil GP, Rondiya SR, Bagal VS, Shivhare S, Cross RW, Dzade NY, Jadkar SR, Chavan PG (2021) Field emission characteristics of double walled TiO_2 nanotubes. ES Mater Manuf 13:76–81
52. Wu N, Du W, Hu Q, Vupputuri S, Jiang Q (2020) Recent development in fabrication of Co nanostructures and their carbon nanocomposites for electromagnetic wave absorption. Engineered Science. https://doi.org/10.30919/es8d1149
53. Fang J, Zhang Y, Zhou Y, Zhao S, Zhang C, Huang M, Gao Y (2017) Synthesis of NiO-TiO_2 hybrids/mSiO_2 yolk-shell architectures embedded with ultrasmall gold nanoparticles for enhanced reactivity. Appl Surf Sci 412:616–626
54. Xu LQ, Jiang H, Neoh K-G, Kang E-T, Fu GD (2012) Poly(dopamine acrylamide)-co-poly(propargyl acrylamide)-modified titanium surfaces for 'click' functionalization. Polym Chem 3(4):920–927
55. Demirci S, Caykara T (2012) High density cationic polymer brushes from combined "click chemistry" and RAFT-mediated polymerization. J Polym Sci, Part A: Polym Chem 50(15):2999–3007
56. Huang F, Guo Y, Wang S, Zhang S, Cui M (2017) Solgel-hydrothermal synthesis of Tb/Tourmaline/TiO_2 nano tubes and enhanced photocatalytic activity. Solid State Sci 64:62–68
57. Liu C, Lin Y, Dong Y, Wu Y, Bao Y, Yan H, Ma J (2020) Fabrication and investigation on Ag nanowires/TiO_2 nanosheets/graphene hybrid nanocomposite and its water treatment performance. Adv Compos Hybrid Mater 3:402–414
58. Kala PV, Srinivasarao K (2019) Structural and luminescence studies on TiO_2-MoO_3 thin films. Adv Compos Hybrid Mater 2(4):735–742
59. Zhou T, Ashley J, Feng X, Sun Y (2018) Detection of hemoglobin using hybrid molecularly imprinted polymers/carbon quantum dots-based nanobiosensor prepared from surfactant-free Pickering emulsion. Talanta 190:443–449
60. Zhao T, Wang J, He J, Deng Q, Wang S (2017) One-step post-imprint modification achieve dual-function of glycoprotein fluorescent sensor by "Click Chemistry." Biosens Bioelectron 91:756–761
61. Cui K, Yan B, Xie Y, Qian H, Wang X, Huang Q, He Y, Jin S, Zeng H (2018) Regenerable urchin-like Fe_3O_4@PDA-Ag hollow microspheres as catalyst and adsorbent for enhanced removal of organic dyes. J Hazard Mater 350:66–75
62. Feng Z, Li Z, Zhang X, Xu G, Zhou N (2018) Fluorescent carbon dots with two absorption bands: luminescence mechanism and ion detection. J Mater Sci 53(9):6459–6470
63. Wu N, Zhao B, Liu J, Li Y, Chen Y, Chen L, Wang M, Guo Z (2021) MOF-derived porous hollow Ni/C composites with optimized impedance matching as lightweight microwave absorption materials. Adv Compos Hybrid Mater 4(3):707–715
64. Reddad Z, Gerente C, Andres Y, Le Cloirec P (2002) Adsorption of several metal ions onto a low-cost biosorbent: kinetic and equilibrium studies. Environ Sci Technol 36(9):2067–2073
65. Kayan A (2018) Inorganic-organic hybrid materials and their adsorbent properties. Adv Compos Hybrid Mater 2(1):34–45
66. Shen W, Chen S, Shi S, Li X, Zhang X, Hu W, Wang H (2009) Adsorption of Cu(II) and Pb(II) onto diethylenetriamine-bacterial cellulose. Carbohydr Polym 75(1):110–114
67. Bhattacharyya KG, Gupta SS (2008) Influence of acid activation on adsorption of Ni(II) and Cu(II) on kaolinite and montmorillonite: kinetic and thermodynamic study. Chem Eng J 136(1):1–13

68. Rao W, Cai R, Chen X, Liu Y, Chen H, Zhang Z, Nie L (2013) Preparation and adsorption properties of novel magnetic tetrabromobisphenol a molecularly imprinted composite material based on graphene oxide surface. Chem J Chin Univ 34(6):1353–1359